Enhanced bacterial chemotaxis in confined microchannels: Optimal performance in lane widths matching circular swimming radius

Caijuan Yue[1,2], Chi Zhang[1,2,*], Rongjing Zhang[1,*], Junhua Yuan[1,*]

[1] Hefei National Research Center for Physical Sciences at the Microscale, and Department of Physics, University of Science and Technology of China, Hefei, Anhui, 230026, China

[2]These authors contributed equally.

*Corresponding authors:

Junhua Yuan, Rongjing Zhang or Chi Zhang, Hefei National Research Center for Physical Sciences at the Microscale, and Department of Physics, University of Science and Technology of China, Hefei, Anhui, 230026, China, email: jhyuan@ustc.edu.cn; rjzhang@ustc.edu.cn; zhchi@ustc.edu.cn

Abstract

Understanding bacterial behavior in confined environments is helpful for elucidating microbial ecology and developing strategies to manage bacterial infections. While extensive research has focused on bacterial motility on surfaces and in porous media, chemotaxis in confined spaces remains poorly understood. Here, we investigate the chemotaxis of *Escherichia coli* within microfluidic lanes under a linear concentration gradient of L-aspartate. We demonstrate that *E. coli* exhibits significantly enhanced chemotaxis in lanes with sidewalls compared to open surfaces. We attribute this phenomenon primarily to the intrinsic chiral clockwise circular motion of surface-swimming bacteria and the subsequent alignment effect upon collision with the sidewalls. By varying lane widths, we identify that an 8 μm width—approximating the radius of bacterial circular swimming on surfaces—maximizes chemotactic drift velocity. These results are supported by both experimental observations and stochastic simulations, establishing a clear proportional relationship between optimal lane width and the radius of bacterial circular swimming. Further geometric analysis provides an intuitive understanding of this phenomenon. Our results may offer insights into bacterial navigation in complex biological environments such as host tissues and biofilms, providing a preliminary step toward exploring microbial ecology in confined habitats and potential strategies for controlling bacterial infections.

Introduction

Microorganisms inhabit a variety of complex confined environments. Sperm swimming in the reproductive tract of a female animal (1), bacteria navigating through host cells and tissues (2), cells moving in the wrinkle of biofilm (3), and swarm cells maneuvering in crowded cell clusters (4) are all examples of organisms operating in geometrically confined environments. Furthermore, many diseases have been found to be related to bacterial motion in confinement, such as urinary tract infections and neonatal sepsis.

Previous research has explored the motion of bacteria in confined environments. Studies have shown that flagellated bacteria tend to accumulate near both solid-liquid (5, 6) and air-liquid interfaces (7), and exhibit a specific chirality in their direction of circular swimming (8). For example, *E. coli* swim clockwise when observed from above a solid surface (8-11), whereas *Caulobacter crescentus* move in tight, counter-clockwise circles when viewed from the liquid side. Moreover, Tang *et al.* found that flagellated bacteria orbit within the thin fluid film around micrometer-sized particles (12). Bacteria also display different motion behaviors in porous media and tubes (13-19), as well as in other types of confinement (20-22). In narrow channels with width less than 4 μm, bacterial growth (23), swimming trajectories (24) and swimming speeds (25) are significantly impacted compared to bulk conditions. Furthermore, studies on bacterial transport in rectangular microchannels under flow have demonstrated that confinement influences both bacterial fluxes and spatial distribution, with cells exhibiting distinct transport dynamics along channel edges (26). However, while motility in confinement is well-documented, the specific rules governing bacterial chemotaxis within geometrically constrained environments remain less understood.

E. coli can sense and move in chemical gradients through a set of chemotactic proteins (27, 28). The transmembrane chemoreceptors detect attractants or repellents and transmit signals into the cell by modulating the autophosphorylation of the histidine kinase CheA. Attractant binding suppresses CheA autophosphorylation, while repellent binding promotes it. This modulation alters the concentration of the phosphorylated response regulator protein, CheY-P (28-31). CheY-P binds to the cytoplasmic domain of flagellar motors, altering the probability of their clockwise rotation (32, 33). Clockwise and counterclockwise rotations of motors lead to reorientation (tumble) and smooth swimming (run) modes of the cell body, respectively (34). The adaptation enzymes CheR and CheB methylate and demethylate the receptors, respectively, mediating sensory adaptation (35, 36).

While the molecular mechanism is well-characterized, the physical environment plays

a crucial role in chemotactic efficiency. Bacterial chemotaxis has been observed under various degrees of confinement, often yielding complex behaviors. For instance, in quasi-2D microchannels with a depth of 2 μm, bacteria were found to adjust their run lengths and tumble frequencies to respond to chemical gradients (37). Similarly, studies in 10 μm-depth microchambers revealed that *E. coli* maintains chemotactic performance in the presence of evenly spaced obstacles (38). While these studies focused on confinement between top and bottom surfaces, recent work by Braham et al showed that bacteria on a single solid surface can exhibit an escape response to high-concentration chemorepellents (250 mM $Ni(NO3)_2$) (39). Conversely, other research has shown that bacterial chemotactic drift velocity decreases sharply near sample chamber surfaces compared to bulk liquid, a phenomenon attributed to circular cell movement at these interfaces (40). This observation suggests that a single surface can significantly impair bacterial chemotactic performance. Yet, a study of chemotaxis in two-dimensional bacterial swarms on semisolid agar surfaces has demonstrated that *E. coli* can exhibit effective chemotaxis in attractant gradients, especially at high cell densities (4). This apparent contradiction is likely due to cell-cell interactions mitigating surface effects in dense populations. Despite these investigations into motility under surface effects, a comprehensive understanding of how specific confinement geometries modulate chemotaxis remains limited.

Here, we study the chemotaxis of *E. coli* on surfaces within lanes of different widths, exposed to a linear concentration gradient of L-aspartate using a hydrogel-based microfluidic device. Our findings reveal enhanced chemotactic performance in the presence of sidewalls compared to their absence. Cells in the middle area (MA) exhibited no drift and did not contribute to overall chemotaxis. However, cells near the left sidewall (LSW) and right sidewall (RSW) demonstrated negative and positive drift, respectively, with the positive drift velocity from the RSW exceeding the negative drift velocity from the LSW.

Furthermore, by comparing lanes of different widths within the same stable linear

gradient field, we observed that cells exhibited the highest drift velocity in 8 μm-wide lanes, which approximates the peak value in the distribution of circular swimming radii on surfaces. This optimal width for maximal chemotaxis resulted from the largest percentage of cells occupying the right sidewalls. Stochastic simulations of bacterial chemotaxis corroborated that the optimized lane width varies with the bacteria's circular swimming radius. Our findings have important implications for the screening of swimming organisms and the study of chemotactic behavior in real-world scenarios.

Results

Chemotaxis of *E. coli* within lane confinements

To study bacterial chemotaxis in confined environments such as tubes or interstitial tissues, we developed a hydrogel-based microfluidic device featuring lanes of different widths. The device design, illustrated in Fig. 1A, incorporates two 2% (w/v) agarose walls inserted between three main channels: a sink channel, a cell channel, and a source channel. These walls prevent cell passage while allowing chemical diffusion. The agarose walls and main channels measure 100 μm and 400 μm in width, respectively, with the device having a depth of 30 μm.

We established a linear concentration gradient (0.05 μM/μm) of L-aspartate, an attractant sensed by the Tar receptor, by flowing motility medium through the sink channel and 50 μM L-aspartate solution (prepared in motility medium) through the source channel at a constant rate of 10 μL/min. The resulting gradient across the cell channel is depicted in Fig. S1.

The lanes of various widths were created using parallel PDMS (polydimethylsiloxane) pillars spaced at different distances. Each lane, approximately 160 μm in length, is highlighted by a yellow rectangular box in Fig. 1A. *E. coli* cells, confined to the cell channel, sensed the attractant gradient and performed chemotaxis within these lanes of different widths.

To enhance imaging contrast, we introduced a plasmid expressing mCherry fluorescent protein (pTrc99a-mcherry) into wild-type *Escherichia coli* HCB1, denoting it as HCB1-pTrc99a-mcherry. A high-sensitivity CMOS camera was used to record bacterial movement trajectories on the bottom surfaces of the lanes in the cell channel, where most cells accumulate due to the combined effects of gravity and hydrodynamic wall attraction in the Percoll-free medium.

We recorded the movement of HCB1-pTrc99a-mcherry cells on the liquid-glass surface of a 44-μm-wide lane with and without a L-aspartate concentration gradient, respectively. An example video is shown in Movie S1, and several representative trajectories are illustrated in Fig. 1B.

Considering the potential escape into the third dimension at the edge (26), we calculated the drift velocities v_d of the trajectories from both assays along the x-direction (up-gradient) by fitting the relation $\langle x(i+n) - x(i)\rangle \sim n\Delta t$ (n=1, 3, 5, …, 39) with a linear function, the slope of which is the drift velocity. Here, $x(i)$ represents the cell's x-position in the i-th frame, and Δt denotes the time interval between two frames (0.05 s). This method yields a drift velocity that is independent of potential cell loss into the third dimension. As shown in Fig. 1C, the drift velocity v_d was 1.6±0.3 μm/s and 0.2 ±0.2 μm/s (mean±SD) for the gradient and control (no-gradient) assays, respectively. Thus, bacteria in the L-aspartate gradient exhibited obvious chemotaxis on the lane surfaces, contrasting with previous findings on liquid-solid surfaces without sidewalls (40).

The cells in the right sidewall region dominated the chemotaxis of *E. coli* within lane confinements.

To elucidate the mechanism of bacterial chemotaxis within lane confinements, we analyzed cell trajectories, identifying three distinct motion states due to the presence of sidewalls. As illustrated in Fig. 2A, cells exhibited straight-line swimming along

sidewalls, movement towards or away from sidewalls, or circular swimming. Fig. 2B displays three representative trajectories. Circular swimming is characteristic of typical *E. coli* surface motion (8). We further analyzed the trajectories of bacteria colliding with the sidewalls. As shown in Fig. S2, cells colliding with the sidewalls tend to align with and swim along the sidewalls, and the alignment timescale is negligible compared to the typical wall residence time (6).

We distinguished these motion states by calculating the rotational exponent (γ_R) for each trajectory, fitting the mean-squared orientational displacement $\langle \mathrm{MSOD} \rangle$ for $\tau < 0.4$ s:

$$\langle \mathrm{MSOD} \rangle = \langle \left(\theta(t+\tau) - \theta(t)\right)^2 \rangle = C_R \tau^{\gamma_R} ,$$

where $\theta(t)$ is the angle between the swimming direction and the positive *x*-axis direction at time *t*, τ is the lag time, C_R is a constant, and γ_R is the rotational exponent. Fig. 2C shows the γ_R values for the three trajectories in Fig. 2B, while Fig. 2D illustrates the relationship between γ_R and average *y*-coordinate. Trajectories further from sidewalls exhibit larger γ_R, indicating more curved paths, while γ_R decreases sharply as the cells approach sidewalls, representing straighter trajectories.

We also analyzed tumble kinematics for cells swimming along and away from sidewalls. Fig. 2E and 2F show normalized tumble angle distributions for cells in sidewalls (SW) and middle areas (MA), respectively. Red solid lines represent exponential function fits $y = a * \exp(x/b)$, with fitted *b* values of 0.25 rad (SW) and 1.35 rad (MA). Consistent with previous reports (41), we observed a higher occurrence of large reorientation angles for surface-swimming cells in the MA region (Fig. 2F). Interestingly, we also found large tumble angles in the SW region, albeit with a smaller characteristic angle than in the MA region. Movie S2 demonstrates an example of a large reorientation angle during tumbling.

Given the strong spatial dependence of trajectory characteristics, we classified the cells

195 into three distinct populations. The distribution of cells along the *y*-axis is shown in Fig.
196 2G. Based on mean distances from the sidewalls, we divided the lane into three areas
197 (viewing along the positive *x*-axis): the left sidewall (LSW), the middle area (MA), and
198 the right sidewall (RSW). As shown by different shaded colors in Fig. 2D and 2G, we
199 defined cells in LSW, RSW and MA for trajectories with $\langle x \rangle \leq d$, $\langle x \rangle \geq w - d$, and
200 $d < \langle x \rangle < w - d$, respectively. The threshold d was set at 3 μm (approximately the
201 average length of a cell body), and w represents the lane width. The proportion of
202 trajectories in different regions is shown in Fig. 2I. For the gradient assay, the
203 probabilities of trajectories being in LSW, MA and RSW regions were 0.20 ± 0.01, 0.59
204 ± 0.02, and 0.21 ± 0.03, respectively. In the control assay without gradient, these values
205 were 0.18 ± 0.03, 0.70 ± 0.03, and 0.12 ± 0.01, respectively.
206
207 We then compared the drift velocity of cells in the three areas separately for both
208 gradient and control assays. As shown in Fig. 2H, cells in the LSW region tended to
209 display a negative drift with v_d^{LSW}= -5.7±2.1 μm/s and -5.0 ± 2.0μm/s for gradient and
210 control assays, respectively. Cells in the MA region exhibited minimal drift with v_d^{MA}=
211 -0.3 ± 1.2 μm/s and 0.4 ± 0.6 μm/s for gradient and control assays, respectively. Cells
212 in the RSW region displayed a typical positive drift with v_d^{RSW}= 14.8 ± 1.2 μm/s and
213 6.2 ± 1.9 μm/s for gradient and control assays, respectively. Thus, cells in the RSW
214 region dominated the difference in drift velocity between the two assays.
215
216 In summary, cells swim on the right-hand side under the effect of the bottom surface of
217 lanes (9) , a behavior fundamentally dictated by the chirality of their surface interaction.
218 The LSW and RSW cells swim down and up the gradient, respectively, while MA cells
219 swim in circles without any drift. RSW cells demonstrated more persistent swimming
220 towards the attractant in the L-aspartate gradient, exhibiting a higher positive drift
221 velocity. To further illustrate the significance of this chirality, consider a hypothetical
222 scenario where the bacteria exhibited counterclockwise circular swimming on the
223 surface. In such a case, the hydrodynamic interaction would cause cells to veer to the
224 left rather than the right. Consequently, the cells swimming up-gradient would

accumulate along LSW, while those swimming down-gradient would accumulate along RSW. While the overall enhancement of chemotaxis via confinement would persist, the spatial distribution of the up- and down-gradient populations would be mirrored relative to the channel axis. Detailed information on the difference in drift velocity between LSW and RSW cells can be found in the supplemental materials. Notably, the attractant gradient minimally affects the ratio of bacteria in different regions.

The dependence of chemotactic performance on lane width

Having established that *E. coli* chemotaxis on lane surfaces is closely related to sidewall confinement, we investigated chemotaxis in lanes of different widths to mimic bacterial chemotactic behavior in interstitial tissues or tubes of varying sizes. We compared five lanes with widths of 6 μm, 8 μm, 10 μm, 25 μm, and 44 μm. Drift velocity was calculated using the same method as in Fig. 1C, with results shown in Fig. 3A. The mean drift velocities were 1.8 ± 1.3 μm/s, 7.5 ± 1.4 μm/s, 4.6 ± 1.7 μm/s, 2.5 ± 0.5 μm/s, and 2.6 ± 0.4 μm/s for lanes of width 6 μm, 8 μm, 10 μm, 25 μm, and 44 μm, respectively. Bacteria exhibited optimal chemotaxis (highest drift velocity) in lanes that were 8 μm wide. To rule out any potential ratchet effect caused by the asymmetric entrances, we performed control measurements using a setup with straight entrances; these results confirmed our findings and are shown in Fig. S3.

Noting that this optimal width is of the same order of magnitude as the radius of bacterial circular swimming on a solid surface, we measured the radius of circular swimming for cells in the MA region. As shown in Fig. 3B, the peak radius in the distribution of circular swimming radii is ~10 μm, which is close to the lane width supporting optimal chemotaxis.

It has been reported that bacteria swimming in capillaries of different radii possess different swimming speeds (42). Therefore, we calculated the cell swimming speeds for all lane widths. As shown in Fig. 3C, swimming speed remains relatively constant across different lane widths. This indicates that the optimized chemotaxis is not a result

of varying swimming speeds.

The optimal chemotaxis resulted from more cells moving towards the attractant along the right sidewall.

To identify the underlying mechanism of optimal lane width for chemotaxis, we evaluated the drift velocity for cells in the LSW, MA, and RSW regions separately. The results are shown in Fig. 4A. Cells in the MA region did not exhibit effective drift, while LSW and RSW cells demonstrated negative and positive drift, respectively, consistent with the findings in Fig. 2H. The drift velocity for RSW cells increased with lane width, and remained relatively constant above a lane width of 8 μm, thus not exhibiting a highest value in the 8 μm-wide lanes. Therefore, the width-dependent optimal chemotaxis is not attributable to an optimal drift velocity for RSW cells.

We then sought a comparison of cell proportions in the three areas, as plotted in Fig. 4B. The proportion of cells in the MA region increased gradually with lane width due to the increase in area. Notably, the largest proportion of RSW cells appears in the 8 μm-wide lane. In other words, the lane width-dependent optimal chemotaxis primarily resulted from changes in cell numbers on the sidewalls. The relation between cell enrichment and lanes' width was plotted in Fig. S4.

To further investigate changes in up- and down-gradient cell numbers in the RSW region, we calculated the proportion of RSW-UG (cells swimming up-gradient in the RSW) and RSW-DG (cells swimming down-gradient in the RSW) cells. As shown in Fig. 4C, more cells moved towards the attractant in the 8 μm-wide lane. Thus, the optimal chemotaxis in the 8 μm-wide lane resulted from a higher number of cells moving towards the attractant along the right sidewall.

Simulation of *E. coli* chemotaxis within lane confinements

To explore the relationship between the circular swimming of bacteria on lane surfaces and optimal chemotaxis, we simulated two-dimensional chemotaxis of bacteria with

varying circular swimming radii on lanes of different widths in a steady linear gradient of L-aspartate.

In our simulation, cells were treated as self-propelled particles performing a random walk in a run-and-tumble mode within a two-dimensional space. Cells could be in either a run or tumble state, determined by the intracellular chemotaxis signal. During a run, cells swam smoothly at a constant speed of v_0=20 μm/s. The effect of the bottom surface on bacterial swimming was modeled by adding a constant angular velocity term to the swimming direction:

$$\theta(t+\Delta t) = \theta(t) + \left(-\frac{v_0}{r}\right)\Delta t + \sqrt{2D_r\Delta t}\, n(0,1)$$

where θ denotes the angle between the swimming direction and the positive x-axis, Δt is the time step, r is the radius of circular swim, D_r is the rotational diffusion coefficient, and $n(0, 1)$ represents a random number drawn from a standard normal distribution. When cells collided with sidewalls, their velocities instantly aligned with the sidewall (43), and could potentially leave the sidewall after their next tumble. During a tumble, cells stopped moving, and their swimming direction changed. The change in θ was selected from the distribution of tumble angles observed in Fig. 2E and F for different areas.

Initially, 100 cells were evenly distributed on the surface of a lane measuring 160 μm in length and w in width. A linear concentration gradient of L-aspartate, identical to the experimental conditions, was established along the x-axis according to:

$$c(x) = 0.05x + 22,$$

with the concentration c in μM and the position x in μm. The simulation for each set of parameters ran for 150 s with a timestep of 0.05 s and was repeated 50 times.

Figure 5A illustrates the relationship between chemotactic drift velocity and lane width for cells with a 10 μm-radius circular swim. The highest drift velocity was observed at a lane width of 8 μm. Figure 5B shows the proportions of cells in the three regions

(LSW, MA, RSW) for different lane widths, presenting profiles similar to those observed experimentally in Fig. 4B. The drift velocity for 3 regions was shown in Fig. S5. Results for different swimming radii are presented in Fig. 5C, demonstrating that the optimal lane width for chemotaxis is closely related to the radius of circular swimming. It is important to note that our model treats bacteria as active particles and does not explicitly account for the steric exclusion of the flagella and cell body. In reality, these effects would restrict the cells' ability to turn freely in narrow lanes (≤ 6 μm), thereby reducing the cell density mismatch between the LSW and RSW and decreasing the drift velocity compared to the simulation. Consequently, the distinct behaviors of the left and right sidewall populations observed in the simulation at very small widths (Fig. 5B) reflect the idealized nature of our model, specifically the absence of steric hindrance.

As shown in Fig. 5D, the relationship between optimal lane width (w) and circular swimming radius (r) was fitted with a linear function $w = kr$, with $k = 0.66 \pm 0.03$. This indicates a clear proportional relationship between the lane width for optimal chemotaxis and the circular swimming radius of bacteria.

Geometrical analysis of optimal lane width for chemotaxis.

We have established that the optimal lane width for chemotaxis (8 μm) primarily results from a higher proportion of cells in the RSW region swimming up-gradient. Additionally, this optimal width is directly proportional to the circular swimming radius of the bacteria. To further elucidate the underlying mechanism of this phenomenon, we employed geometrical analysis.

We assumed an initial uniform distribution of cells across the lane width. As shown in Fig. 6A-C, we divide the width of the lane into three scenarios:

1. $0 < w \leq r$: For a cell at any point P in the channel, its swimming direction can be arbitrary. However, only cells swimming in directions between θ_1 and θ_2 (highlighted in green) can swim up-gradient in the RSW after their first collision with

the sidewall. The proportion of these cells can be calculated as:

$$\frac{1}{w}\int_0^w \frac{\theta_1+\theta_2}{2\pi}dy = \frac{1}{2\pi w}\int_0^w dy\left(\operatorname{acos}\frac{r-w+y}{r} + \operatorname{acos}\frac{y}{r}\right)$$
$$= \frac{1}{2\pi m}\left[-(1-m)\operatorname{acos}(1-m) + \sqrt{1-(1-m)^2} + m\operatorname{acos} m - \sqrt{1-m^2} + 1\right],$$

where $m = w/r \leq 1$.

2. $r < w \leq 2r$: Only the cells in the region $y < r$ and with velocity direction between θ_1 and θ_2 can swim up-gradient in the RSW after their first collision with the sidewall. The proportion of cells in this region is:

$$\frac{1}{w}\int_0^r \frac{\theta_1+\theta_2}{2\pi}dy = \frac{1}{2\pi w}\int_0^r dy\left(2\operatorname{acos}\frac{y}{r}\right) = \frac{1}{\pi m}$$

3. $w > 2r$: The proportion of cells that can swim up-gradient in the RSW is calculated the same as in case 2:

$$\frac{1}{w}\int_0^r \frac{\theta_1+\theta_2}{2\pi}dy = \frac{1}{\pi m}$$

The complete relationship between the proportion of cells that can swim up-gradient in the RSW (*P*) and *m* is plotted in Fig. 6D. The maximum *P* occurs when $m \in (0.7, 0.8)$, marked by the red shaded area. This value is consistent with the slope *k* in Fig. 5D and results in the optimal width of about 8 μm in Fig. 3A for a circular swimming radius of 10 μm.

Crucially, the observed asymmetry arises because the angular ranges that geometrically facilitate RSW-UG accumulation (Fig. 6A-C) coincide with the up-gradient direction. Because cells moving up-gradient experience suppressed tumbling, they can maintain the steady circular trajectories required to reach and align with the RSW. Conversely, while a pure geometric analysis suggests a symmetric potential for LSW-DG accumulation, these trajectories coincide with the down-gradient direction. Consequently, these cells experience enhanced tumbling, which distorts the circular

trajectories. This prevents them from effectively reaching the LSW and also increases the probability of them leaving the wall.

Discussions

Bacterial behavior in confined environments differs significantly from that in free environments. Previous studies have reported that cells tend to swim in circles and accumulate near a solid-liquid interface, leading to diminished chemotaxis. However, recent research on chemotaxis of swarm cells suggests that crowded environments may enhance bacterial chemotaxis on surfaces. In this study, we examined the chemotaxis of *E. coli* on the bottom surface of microfluidic lanes, which simulate the spatial constraints imposed by neighboring cells in a swarm, exploring the effects of lane confinement on bacterial chemotaxis.

We found that in the presence of sidewalls, cells that would otherwise have been unable to exhibit chemotaxis showed significant chemotactic behavior in a linear gradient of L-aspartate. Cells in different regions of the lanes demonstrated distinct motion behaviors. In the MA region, cells showed no drift, similar to observations in chemotaxis near surfaces. Conversely, cells exhibited positive and negative drift when in the RSW and LSW regions, respectively.

Further investigation into chemotaxis in lanes of varying widths demonstrated that cells exhibited the highest chemotactic drift velocity in lanes that were 8 μm wide. This width is close to the radius of bacterial swimming circles. By analyzing the proportion and drift velocity of cells in different regions, we determined that this optimal lane width was primarily due to the higher proportion of cells swimming up-gradient along the right sidewall.

To explore the relationship between chemotactic drift velocity and circular swimming radius of bacteria, we conducted systematic simulations of *E. coli* chemotaxis with

different circular swimming radii in lanes of varying widths under a linear concentration gradient of L-aspartate. These simulations explicitly incorporated the chiral clockwise circular motion of surface-swimming bacteria and the alignment effect induced by sidewall collisions. We found that optimal chemotaxis occurred when the swimming radius was close to the lane width, with $w = 0.66r$. This suggests a significant proportional relationship between the optimal lane width for chemotaxis and the circular swimming radius of bacteria.

To elucidate the mechanism underlying this phenomenon, we employed geometric analysis. We demonstrated that bacteria in lanes could swim up-gradient in the RSW with maximal probability when the lane width was 0.7-0.8 times the radius of circular swimming. This finding is consistent with the experimental results presented in Fig. 4C.

Our findings have important implications for the screening of single-celled swimming organisms and the study of restricted chemotactic behavior. This research provides insights into how confinement affects bacterial chemotaxis and may inform the design of microfluidic devices for bacterial manipulation and analysis.

Bacteria frequently inhabit confined spaces such as soil pores, sediment interstices, rock crevices, biological tissues, and hydrogels. In these constrained environments, bacterial behavior often deviates significantly from that observed in unconfined conditions, typically resulting in reduced chemotactic ability. However, our findings challenge this notion, suggesting that certain types of environmental confinement may actually enhance bacterial chemotaxis. This discovery could contribute to our understanding of microbial ecology across various habitats, including soil, oceans, and the human body.

Furthermore, these insights could have potential applications. In biotechnology, optimizing confinement conditions could improve the efficiency of bioremediation processes or the production of microbial products. In medicine, understanding how pathogens navigate confined spaces within the body could lead to novel strategies for

431 preventing or treating infections.

432

433 ## Materials and methods

434 ### Strain and plasmids

435 The plasmid pTrc99a-mCherry expresses mCherry under an IPTG-inducible promoter.
436 The wild-type *E. coli* K12 strain AW405 (HCB1) transformed with pTrc99a-mCherry
437 was used for fluorescent tracking of cell trajectories. Cells were streaked on a Petri dish
438 containing 1.5% agar and lysogeny broth (1% tryptone, 0.5% NaCl, 0.5% yeast extract,
439 supplemented with the appropriate antibiotic: 100 μg/ml ampicillin). A single colony
440 was inoculated into lysogeny broth and grown overnight at 33 °C with 200 rpm rotation.
441 The saturated culture was then diluted 1:100 (100 μl in 10 ml) into tryptone broth (1%
442 tryptone, 0.5% NaCl, supplemented with the appropriate inducer and antibiotic: 0.1
443 mM IPTG, 100 μg/ml ampicillin) and grown at 33 °C with 200 rpm rotation to
444 OD_{600}=0.53. Cells were then harvested from culture media by centrifugation at 1.2×g
445 for 6 min at room temperature. The pellet was resuspended by gently mixing in motility
446 medium (10 mM potassium phosphate, 0.1 mM ethylenediaminetetraacetic acid
447 (EDTA), 10 mM lactic acid, and 1 μM methionine at pH 7.0). The cells were washed
448 three times to replace growth medium with motility medium. One hour after
449 fluorescence maturation in a 33°C incubator, cells were placed in a 4°C refrigerator
450 ready for microfluidic experiments.

451

452 ### Microfluidic device design and fabrication

453 A hydrogel-based microfluidic device containing lanes of different width was designed
454 using L-edit based on previous work (42). The silicon mold with the positive relief
455 features was fabricated using the standard soft lithography technique performed in our
456 laboratory. Firstly, a 4-inch diameter silicon wafer was spin washed sequentially using
457 water, acetone, methanol and isopropanol. The wafer was thoroughly dried on a 150 °C
458 hot plate to ensure that organics has volatilized completely. Then, the wafer was treated
459 with air plasma (Harrick plasma, PDC-002, 30W) for 10 min before the SU-8 2025

460 photoresist (Microchem) was spin-coated according to the products protocols. The spin-
461 coated wafer was placed on a hot plate at 65°C for 3 min followed by 6 min at 95°C,
462 then exposed to UV light using a maskless lithography machine (Heidelberg, μMLA)
463 at 800 mJ/cm^2 with defocus was set to 0. The post-exposure bake was performed at 65°C
464 for 2 min followed by 6 min at 95°C. Development procedure lasted about 6 minutes
465 with constant shaking in the SU-8 developer. The wafer was rinsed with fresh developer
466 followed by isopropanol. Finally, an approximately 30-μm-high photoresist layer was
467 created as the master mold. The mold was fixed on a glass petri dish using double-sided
468 tape.
469
470 Polydimethylsiloxane (PDMS) and curing agent was mixed with a 10:1 ratio (Sylgard
471 184, Dow Corning) and centrifuged at 3500 rpm for 5 min to remove air bubbles. The
472 mixture was poured over the mold in glass petri dish and then placed at 4°C for an hour
473 to avoid interference from very small air bubbles. The PDMS was cured at 80°C for 3
474 h, then separated from the wafer and cut into pieces, and holes were punched for inlets
475 and outlets. The punched PDMS was cleaned with adhesive tape. The cleaned PDMS
476 was bonded to a glass slide after air plasma treatment (Harrick plasma, PDC-002, 30W).
477 The fabricated device was baked at 80°C overnight to establish covalent bonding.
478
479 The hydrogel agarose was used at 2% (w/v) concentration in motility medium to create
480 diffusion-permeable walls. Agarose was slowly injected through the inlet port using a
481 syringe pump at a constant flow rate of 2 μL/min, and the injection process was carried
482 out in a drying oven at a constant temperature of 68 °C.
483
484 **Microscopy and data acquisition**
485 The PDMS microfluidic chip was placed on a Nikon Ti-E inverted optical microscope
486 equipped with a specific filter set, a 20× objective (Nikon, CFI S Plan Fluor ELWD,
487 20×, NA 0.45), and a CMOS camera (Hamamatsu, ORCA-Flash4.0, pixel size = 6.5
488 μm). We set the objective lens's correction collar to 1.2 mm to match the glass slide
489 thickness. A halogen lamp serves as the bright-field light source to help locate the

490 observation area, while a xenon lamp serves as the excitation light source for
491 fluorescence experiments. The depth of field is 3.7 μm.

492 **1) Gradient profile calibration**

493 Fluorescein solution (Sigma) was used for visualizing the chemical concentration field
494 in the microfluidic device. 100 μM fluorescein and motility medium were flowed into
495 the source and sink channels respectively, at a constant flow rate of 10 μL/min. One
496 fluorescent image was captured per minute. To avoid the impact of photobleaching on
497 the results, we only illuminated the sample during the imaging process.

498

499 **2) Chemotaxis assays**

500 The aspartic acid and motility medium solutions were respectively introduced into the
501 source and sink channels, and left for more than 1 hour to allow aspartic acid to diffuse
502 through the agarose wall and form a stable concentration gradient field. Then, bacteria
503 were introduced into the cell channel at a rate of 5 μL/min using a syringe pump for a
504 duration of 90 seconds. After the bacteria injection was complete, the microvalves were
505 closed to seal the cell channel. Bacteria then performed chemotaxis due to the
506 perception of the concentration gradient field. After waiting for 2 minutes, the shutter
507 was opened to illuminate the fluorescent bacteria with the excitation light, and video
508 recording began. During the video acquisition process, fluorescence excitation light
509 was continuously illuminated onto the bacteria. For each recording, 9600 frames
510 (2048×2048 pixels) were captured at a frame rate of 20 fps and an exposure of 50 ms.
511 Although the long-term illumination caused a decrease in the brightness of the
512 fluorescent bacteria, the position information of the bacteria could still be accurately
513 distinguished within the video duration (8 min).

514

515 **Data analysis**

516 **Tracking.** Image analysis was performed with the ImageJ (National Institutes of Health)
517 TrackMate plugin. We chose the Log detector with an estimated blob diameter of 70
518 μm and a threshold of 800 μm to effectively recognize bacteria, based on the diameter
519 of bacteria and the use of a 20× objective. Then, we used the LAP Tracker and set the

maximum distance for frame-to-frame linking to 50 μm.

Swimming speed. The velocity is calculated using the fourth order central difference method by (44):

$$\vec{v}_i = \frac{8(\vec{x}_{i+1} - \vec{x}_{i-1}) - (\vec{x}_{i+2} - \vec{x}_{i-2})}{12T}$$

The magnitude of the velocity is given by $v_i = |\vec{v}_i|$. The speed of each trajectory is defined as the average of v_i. The swimming speeds of bacteria in lanes of different widths are represented by the mean and standard deviation of all trajectories.

Calculation of the radius of circular motion on the solid surface. A total of 382 trajectories with a rotational exponent greater than 1.6 in the MA region of the w = 44 μm lanes were selected for analysis. The trajectories were smoothed using the Savitzky-Golay filter with a window size of 5. The least squares method was then applied to solve the linear equations, yielding the center and radius of the fitted circles. The principle of this process is briefly described as follows:

The standard equation of a circle can be written as:

$$(x - a)^2 + (y - b)^2 = r^2,$$

where (a, b) are the coordinates of the circle's center, and r is the radius. Expanding and rearranging the standard equation of a circle, it can be rewritten as:

$$x^2 + y^2 = 2ax + 2by + c,$$

where $\mathrm{c} = r^2 - a^2 - b^2$.

Rewriting the above equation in matrix form, we have:

$$\mathrm{B} = \mathrm{A} \cdot Coefficients$$

where

$$\mathrm{B} = x^2 + y^2 = \begin{bmatrix} x_1^2 + y_1^2 \\ x_2^2 + y_2^2 \\ \vdots \\ x_n^2 + y_n^2 \end{bmatrix}$$

is the response vector, and

$$A = [x \quad y \quad 1] = \begin{bmatrix} x_1 & y_1 & 1 \\ x_2 & y_2 & 1 \\ \vdots & \vdots & \vdots \\ x_n & y_n & 1 \end{bmatrix}$$

is the design matrix. The coefficients are given by:

$$Coefficients = \begin{bmatrix} 2a \\ 2b \\ c \end{bmatrix} = (A^T A)^{-1}(A^T B).$$

Tumble angle. A tumble is defined as points where the velocity is lower than the average velocity of the trajectory $\langle v_i \rangle$ and shows a substantial drop from the previous time point. Specifically, a tumble is identified when:

$$\{v_{t1}, \cdots, v_{tn}\} < \langle v_i \rangle,$$

$$\{v_{t0} - v_{t1}, \ldots, v_{tn-1} - v_{tn}\} > \langle v_i \rangle \cdot \alpha,$$

where $n \geq 2, \alpha = 1/6$ is the threshold, and t_1 and t_n represent the start and end times of a tumble, respectively.

Simulation of bacterial chemotaxis within lanes.

In our simulation, we introduced the effects of bottom surface and sidewalls into the 2-dimensional chemotaxis of *E. coli*. The simulations were carried out in a rectangular area of size 160 μm × *w*, where *w* denotes the lane width. Cells were treated as self-propelled particles. They could sense and adapt to the ligand in the surrounding environment via the intracellular chemotaxis signaling pathway, which could be described by a coarse-grained model of bacterial chemotaxis (45, 46):

$$a = \frac{1}{1 + \exp\left(N\left(\alpha(m - m_0) + \ln\frac{1 + \frac{c}{K_{off}}}{1 + \frac{c}{K_{on}}}\right)\right)},$$

$$\frac{\mathrm{d}m}{\mathrm{dt}} = k_R(1 - a) - k_B a,$$

where a, m, and c represent the activity of the receptor-kinase complex, the methylation level of receptors, and the ligand concentration, respectively. *N* denotes the number of chemoreceptors in a Monod-Wyman-Changeux cluster (47). The values of

parameters we used were the same as before (4, 47, 48): $N = 4.6$, $K_{off} = 1.7\ \mu\text{M}$, $K_{on} = 12\ \mu\text{M}$, $\alpha = 1.7$, $m_0 = 1.0$, $k_R = 0.005\ \text{s}^{-1}$, $k_B = 0.010\ \text{s}^{-1}$.

The concentration of CheY-P, which changes due to the receptor-kinase phosphorylation on CheY, could be calculated by $Y\text{p} = 7.86a$. Consequently, the CW bias (B) of flagellar motors would also vary (49):

$$B = \frac{(Y\text{p})^{10.3}}{(Y\text{p})^{10.3} + 3.1^{10.3}}.$$

It has been reported that the average run time in the near-surface region for wildtype cells is ~2.0 s (corresponding to a run-to-tumble rate of ~0.5 s^{-1}) (11), and the steady-state motor CW bias is ~0.15 without a gradient. The run-to-tumble rate k was set to be equivalent to the motor CCW-to-CW switching rate. As this rate increases linearly with motor bias B (50), it was calculated using $k = \frac{B}{0.31}\ \text{s}^{-1}$. The switching rate from tumble to run was 5 s^{-1} due to the constant tumble duration of 0.2 s (51).

In this way, the motion states of each cell at any moment are determined. During a run, cells swim smoothly with a constant speed of 20 μm/s, influenced by rotational diffusion and the effect of the bottom surface on bacterial swimming:

$$\theta(t + \Delta t) - \theta(t) = \left(-\frac{v_0}{r}\right)\Delta t + n(0, 2D_r\Delta t),$$

$$x(t + \Delta t) - x(t) = v_0 \cos\theta\, \Delta t,$$

$$y(t + \Delta t) - y(t) = v_0 \sin\theta\, \Delta t,$$

where θ is the angle between the swimming direction and the positive x-axis, $v_0 = 20\ \mu\text{m/s}$ is the swimming speed, r is the radius of circular swimming due to the effect of the bottom surface, and $n(0, 2D_r\Delta t)$ represents a normal distribution with zero mean and variance $2D_r\Delta t$. The rotational diffusion coefficient was 0.062 rad^2/s (52). During a tumble, cells stop swimming and a tumble angle is selected from the distribution that we measured (Fig. 2E). We also imposed a maximum detention time limit which, when combined with the variable tumble rate, results in an average wall residence time of approximately 2 s, matching our experimental observations (Fig. S6B). Cells will get a random y-coordinate at the other side when they swim through

the x boundary.

References

1. S. S. Suarez, A. A. Pacey, Sperm transport in the female reproductive tract. *Hum. Reprod. Update* **12**, 23-37 (2005).
2. D. Bray, *Cell Movements: From Molecules to Motility* (Routledge, 1992).
3. S. Geisel, E. Secchi, J. Vermant, The role of surface adhesion on the macroscopic wrinkling of biofilms. *eLife* **11** (2022).
4. M. Tian, C. Zhang, R. Zhang, J. Yuan, Collective motion enhances chemotaxis in a two-dimensional bacterial swarm. *Biophys J* **120**, 1615-1624 (2021).
5. A. P. Berke, L. Turner, H. C. Berg, E. Lauga, Hydrodynamic attraction of swimming microorganisms by surfaces. *Phys. Rev. Lett.* **101**, 038102 (2008).
6. G. Li, J. X. Tang, Accumulation of microswimmers near a surface mediated by collision and rotational brownian motion. *Phys. Rev. Lett.* **103**, 078101 (2009).
7. M. Michael, H. Athena, L. Guanglai, R. M. Martin , X. T. Jay Molecular Adsorption Steers Bacterial Swimming at the Air/Water Interface. *Biophys J* **105**, 21-28 (2013).
8. L. Eric, R. D. Willow, M. W. George, A. S. Howard, Swimming in Circles: Motion of Bacteria near Solid Boundaries. *Biophys J* **90**, 400-412 (2006).
9. W. R. DiLuzio *et al.*, *Escherichia coli* swim on the right-hand side. *Nature* **435**, 1271-1274 (2005).
10. G. Junot *et al.*, Run-to-Tumble Variability Controls the Surface Residence Times of *E. coli* Bacteria. *Phys. Rev. Lett.* **128**, 248101 (2022).
11. M. Molaei, M. Barry, R. Stocker, J. Sheng, Failed escape: solid surfaces prevent tumbling of *Escherichia coli*. *Phys. Rev. Lett.* **113**, 068103 (2014).
12. G. Araujo, W. Chen, S. Mani, J. X. Tang, Orbiting of Flagellated Bacteria within a Thin Fluid Film around Micrometer-Sized Particles. *Biophys J* **117**, 346-354 (2019).
13. T. Bhattacharjee, S. S. Datta, Bacterial hopping and trapping in porous media. *Nat. Commun.* **10**, 2075 (2019).
14. T. Bhattacharjee, S. S. Datta, Confinement and activity regulate bacterial motion in porous media. *Soft Matter* **15**, 9920-9930 (2019).
15. Nicholas A. Licata, B. Mohari, C. Fuqua, S. Setayeshgar, Diffusion of Bacterial Cells in Porous Media. *Biophys J* **110**, 247-257 (2016).
16. D. Shrestha *et al.*, Bacterial mobility and motility in porous media mimicked by microspheres. *Colloids Surf. B* **222**, 113128 (2023).
17. N. Figueroa-Morales *et al.*, *E. coli* "super-contaminates" narrow ducts fostered by broad run-time distribution. *Sci. Adv.* **6**, eaay0155 (2020).
18. H. Wioland, E. Lushi, R. E. Goldstein, Directed collective motion of bacteria under channel confinement. *New J. Phys.* **18**, 075002 (2016).
19. V. Tokárová *et al.*, Patterns of bacterial motility in microfluidics-confining environments. *Proc. Natl. Acad. Sci. U.S.A* **118**, e2013925118 (2021).
20. P. C. Mushenheim, R. R. Trivedi, H. H. Tuson, D. B. Weibel, N. L. Abbott, Dynamic self-assembly of motile bacteria in liquid crystals. *Soft Matter* **10**, 88-95 (2014).
21. C. J. Woolverton, E. E. Gustely, L. Li, O. D. Lavrentovich, Liquid crystal effects on bacterial

643 viability. *Liq. Cryst.* **32**, 417 - 423 (2005).
644 22. X. Chen, R. Zhang, J. Yuan, Vertical confinement enhances surface exploration in bacterial
645 twitching motility. *Environ. Micriobiol.* **26**, e16679 (2024).
646 23. J. Männik, R. Driessen, P. Galajda, J. E. Keymer, C. Dekker, Bacterial growth and motility in sub-
647 micron constrictions. *Proc. Natl. Acad. Sci. U.S.A* **106**, 14861-14866 (2009).
648 24. B. L. Jonathan *et al.*, Transitioning to confined spaces impacts bacterial swimming and escape
649 response. *Biophys J* **121**, 2653-2662 (2022).
650 25. G. Vizsnyiczai *et al.*, A transition to stable one-dimensional swimming enhances E. coli motility
651 through narrow channels. *Nat. Commun.* **11**, 2340 (2020).
652 26. N. Figueroa-Morales *et al.*, Living on the edge: transfer and traffic of E. coli in a confined flow.
653 *Soft Matter* **11**, 6284-6293 (2015).
654 27. G. L. Hazelbauer, J. J. Falke, J. S. Parkinson, Bacterial chemoreceptors: high-performance
655 signaling in networked arrays. *Trends Biochem. Sci.* **33**, 9-19 (2008).
656 28. V. Sourjik, Receptor clustering and signal processing in E. coli chemotaxis. *Trends Microbiol.* **12**,
657 569-576 (2004).
658 29. A. I. M. Salah Ud-Din, A. Roujeinikova, Methyl-accepting chemotaxis proteins: a core sensing
659 element in prokaryotes and archaea. *Cell. Mol. Life Sci.* **74**, 3293-3303 (2017).
660 30. J. J. Falke, G. L. Hazelbauer, Transmembrane signaling in bacterial chemoreceptors. *Trends*
661 *Biochem. Sci.* **26**, 257-265 (2001).
662 31. A. Bren, M. Eisenbach, How Signals Are Heard during Bacterial Chemotaxis: Protein-Protein
663 Interactions in Sensory Signal Propagation. *J. Bacteriol.* **182**, 6865-6873 (2000).
664 32. M. K. Sarkar, K. Paul, D. Blair, Chemotaxis signaling protein CheY binds to the rotor protein FliN
665 to control the direction of flagellar rotation in *Escherichia coli*. *Proc. Natl. Acad. Sci. U.S.A* **107**,
666 9370-9375 (2010).
667 33. G. H. Wadhams, J. P. Armitage, Making sense of it all: bacterial chemotaxis. *Nature reviews.*
668 *Molecular cell biology* **5**, 1024-1037 (2004).
669 34. M. D. Baker, P. M. Wolanin, J. B. Stock, Signal transduction in bacterial chemotaxis. *Bioessays*
670 **28**, 9-22 (2006).
671 35. K. Oosawa, Y. Imae, Demethylation of methyl-accepting chemotaxis proteins in *Escherichia coli*
672 induced by the repellents glycerol and ethylene glycol. *J. Bacteriol.* **157**, 576-581 (1984).
673 36. R. M. Weis, S. Chasalow, D. E. Koshland, Jr., The role of methylation in chemotaxis. An
674 explanation of outstanding anomalies. *The Journal of biological chemistry* **265**, 6817-6826
675 (1990).
676 37. M. R. Raza, J. E. George, S. Kumari, M. K. Mitra, D. Paul, Anomalous diffusion of E. coli under
677 microfluidic confinement and chemical gradient. *Soft Matter* **19**, 6446-6457 (2023).
678 38. S. Rashid *et al.*, Adjustment in tumbling rates improves bacterial chemotaxis on obstacle-laden
679 terrains. *Proc. Natl. Acad. Sci. U.S.A* **116**, 11770-11775 (2019).
680 39. A. Braham *et al.*, Surface conversion of the dynamics of bacteria escaping chemorepellents.
681 *Eur. Phys. J. E* **47**, 56 (2024).
682 40. M. Grognot, K. M. Taute, A multiscale 3D chemotaxis assay reveals bacterial navigation
683 mechanisms. *Commun. Biol.* **4**, 669 (2021).
684 41. L. Lemelle *et al.*, Tumble Kinematics of Escherichia coli near a Solid Surface. *Biophys J* **118**,
685 2400-2410 (2020).
686 42. L. Ping, V. Wasnik, E. Emberly, Bacterial motion in narrow capillaries. *FEMS Microbiol. Ecol* **91**

2, 1-7 (2015).

43. A. Tao, G. Liu, R. Zhang, J. Yuan, Bacteria Optimize Tumble Bias to Strategically Navigate Surface Constraints. *Adv. Sci.* **12**, e02063 (2025).

44. L. Turner, L. Ping, M. Neubauer, H. C. Berg, Visualizing Flagella while Tracking Bacteria. *Biophys J* **111**, 630-639 (2016).

45. L. Jiang, Q. Ouyang, Y. Tu, Quantitative Modeling of *Escherichia coli* Chemotactic Motion in Environments Varying in Space and Time. *PLoS Comput Biol* **6**, e1000735 (2010).

46. Y. Tu, T. S. Shimizu, H. C. Berg, Modeling the chemotactic response of *Escherichia coli* to time-varying stimuli. *Proc. Natl. Acad. Sci. U.S.A* **105**, 14855-14860 (2008).

47. N. Vladimirov, L. Løvdok, D. Lebiedz, V. Sourjik, Dependence of bacterial chemotaxis on gradient shape and adaptation rate. *PLoS Comput Biol* **4**, e1000242 (2008).

48. S. Ren, C. Zhang, R. Zhang, The effect of receptor interaction on the bacterial chemotactic adaptation rate. *JUSTC* **53**, 0703 (2023).

49. P. Cluzel, M. Surette, S. Leibler, An Ultrasensitive Bacterial Motor Revealed by Monitoring Signaling Proteins in Single Cells. *Science* **287**, 1652-1655 (2000).

50. R. He, R. Zhang, J. Yuan, Noise-Induced Increase of Sensitivity in Bacterial Chemotaxis. *Biophys. J.* **111**, 430-437 (2016).

51. H. C. Berg, D. A. Brown, Chemotaxis in Escherichia coli analysed by Three-dimensional Tracking. *Nature* **239**, 500-504 (1972).

52. N. Vladimirov, D. Lebiedz, V. Sourjik, Predicted auxiliary navigation mechanism of peritrichously flagellated chemotactic bacteria. *PLoS Comput Biol* **6**, e1000717 (2010).

Acknowledgements. This work was supported by National Natural Science Foundation of China Grants (12090053, 12474204, and 12104436), Fundamental and Interdisciplinary Disciplines Breakthrough Plan of the Ministry of Education of China (JYB2025XDXM502), University of Science and Technology of China Research Funds of the Double First-Class Initiative (YD2030002501), and a grant from the Ministry of science and technology of China (2019YFA0709303).

Author Contributions. J. Y., R.Z., and C. Z. designed the work. C. Z. and C. Y. performed the experiments. All authors wrote the manuscripts.

Competing financial interests. The authors declare no competing financial interests.

Figure Legends

Fig. 1. **A.** Microfluidic device used in the experiment (top view). **B.** Thirty bacterial trajectories selected from the data of 44-μm-wide lane in gradient assays. Distinct colors denote individual trajectories, with color intensity darkening to indicate time progression. These represent a subset of the trajectories analyzed in panel **C**. **C.** The relationship between Δx and nΔt calculated from all trajectories in the lanes with a width of 44 μm. The black dots represent the gradient assay (∇c=0.05 μM/μm) with a total of 3206 tracks from 6 movies, while the gray dots represent no gradient (∇c=0) with a total of 4755 tracks from 10 movies. The light-yellow and light-blue shadows represent the standard error of the mean (SEM) of different trajectories in the gradient assays and the control assays, respectively. Linear fitting was performed to obtain V_d = 1.6 ± 0.3 μm/s (black solid line) and V_d = 0.2 ± 0.2 μm/s (gray solid line) for gradient and control assays respectively. Error in drift velocity represents standard deviation.

Fig. 2. **A.** Schematic drawing of three typical motion states. **B.** Trajectories for three typical motion states. Red dots represent the start of each trajectory. **C.** Calculating the rotational exponent for each trajectory, γ_R, by fitting the mean-squared orientational displacement $\langle \mathrm{MSOD} \rangle$. Dots were experimental data calculated from the tracks in Fig. 2B. Solid lines were fitting results with $\langle \mathrm{MSOD} \rangle = C_R \tau^{\gamma_R}$. The fitted γ_R values are 0, 0.77, and 1.80 for gray, brown, and black tracks, respectively. **D.** Relationship between the rotational exponent γ_R and the mean y position of the bacterial trajectories. Errors denote SEM. Red and purple shaded area represent the region 3 μm from the LSW and RSW, respectively. Green shaded area represents the MA region. **E&F.** Normalized distribution of tumble angle for tracks along the sidewalls (**E**) and in the MA region (**F**). Red solid lines are fitting results with an exponential function: $y = a * \exp(x/b)$. **G.** Distribution of bacteria along the y-axis in the lanes with a width of 44 μm. The shades of different colors denote the same meaning as in Fig. 2D. **H.** Drift velocity of bacterial cells in the three regions. **I.** Proportions of bacterial trajectories in the three regions. Errors are standard deviations (SD).

Fig. 3. **A.** The drift velocity for the experiments in lanes of different widths. The error in drift velocity is the standard deviation. **B.** The distribution of the radius of circular swimming from 382 trajectories in the MA regions. The peak value of the radius is ~10 μm. **C.** The swimming speed of cells in lanes with different widths. The mean swimming speeds and standard deviations for lanes with widths of 6 μm, 8 μm, 10 μm, 15 μm, 25 μm, and 44 μm are 22.7 ± 8.7 μm/s, 25.4 ± 7.7 μm/s, 27.1 ± 7.9 μm/s, 21.9 ± 7.8 μm/s, 22.1 ± 7.7 μm/s, and 22.6 ± 7.5 μm/s, respectively.

Fig. 4. **A.** Mean drift velocities in the LSW, MA, and RSW regions of lanes with different widths. The errors are SD. **B.** The proportion of bacterial cells in the LSW, MA, and RSW regions of lanes with different widths. Errors represent SD. **C.** The proportion of RSW-UG (cells swimming up-gradient in the RSW) and RSW-DG (cells swimming down-gradient in the RSW) for lanes with different widths.

Fig. 5. Simulation of bacterial chemotaxis on the surface of lanes. **A.** The relationship between drift velocity V_d of cells with 10 μm-radius circular swim and the lane width w. Errors denote SEM. **B.** The proportion of bacterial trajectories in the LSW, MA, and RSW regions of lanes with different widths, for cells with 10 μm-radius circular swim. **C.** The drift velocity V_d of cells with different radii of circular swim in lanes of different widths. **D.** The relationship between circular swim radius and lane width for optimal chemotaxis (maximal drift velocity) in Fig. 5C. The widths were extracted by fitting the peak value of w in Fig. 5A with a gaussian function. The red solid line represents a linear fit. The slope is 0.66 ± 0.03. Errors denote SD.

Fig. 6. Geometrical analysis of optimal lane width for chemotaxis. **A.** Case 1: $0 < w \leq r$. **B.** Case 2: $r < w \leq 2r$. **C.** Case 3: $w > 2r$. The red arrows denote the velocity direction. The black solid lines represent the sidewalls. Dashed circles are trajectories. The up-gradient direction is along the positive x-axis. The green shade areas label the swim direction of cells that can swim up-gradient in the RSW. **D.** Relationship between

probability (P) of cells swimming up-gradient in the RSW and m, where $m = w/r$. Red shaded area denotes m for maximal P, $m \in (0.7,0.8)$.

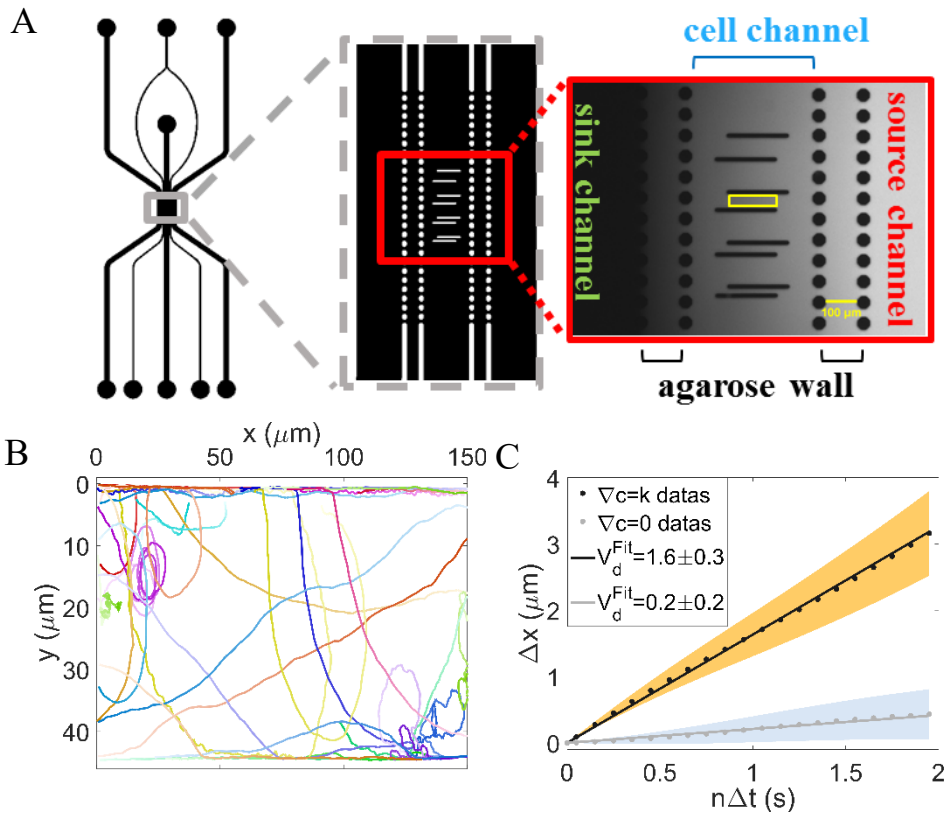

Fig. 1. **A.** Microfluidic device used in the experiment (top view). **B.** Thirty bacterial trajectories selected from the data of 44-μm-wide lane in gradient assays. Distinct colors denote individual trajectories, with color intensity darkening to indicate time progression. These represent a subset of the trajectories analyzed in panel **C**. **C.** The relationship between Δx and nΔt calculated from all trajectories in the lanes with a width of 44 μm. The black dots represent the gradient assay (∇c=0.05 μM/μm) with a total of 3206 tracks from 6 movies, while the gray dots represent no gradient (∇c=0) with a total of 4755 tracks from 10 movies. The light-yellow and light-blue shadows represent the standard error of the mean (SEM) of different trajectories in the gradient assays and the control assays, respectively. Linear fitting was performed to obtain V_d = 1.6 ± 0.3 μm/s (black solid line) and V_d = 0.2 ± 0.2 μm/s (gray solid line) for gradient and control assays respectively. Error in drift velocity represents standard deviation.

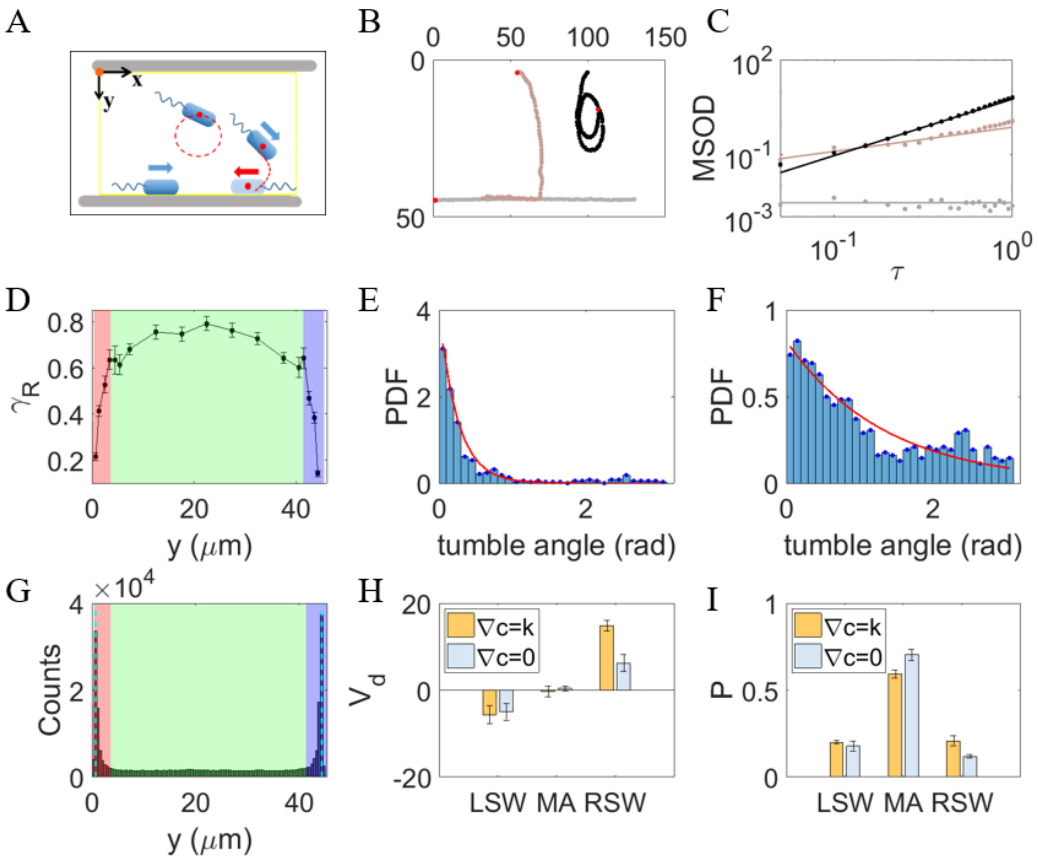

Fig. 2. **A.** Schematic drawing of three typical motion states. **B.** Trajectories for three typical motion states. Red dots represent the start of each trajectory. **C.** Calculating the rotational exponent for each trajectory, γ_R, by fitting the mean-squared orientational displacement $\langle \mathrm{MSOD} \rangle$. Dots were experimental data calculated from the tracks in Fig. 2B. Solid lines were fitting results with $\langle \mathrm{MSOD} \rangle = C_R \tau^{\gamma_R}$. The fitted γ_R values are 0, 0.77, and 1.80 for gray, brown, and black tracks, respectively. **D.** Relationship between the rotational exponent γ_R and the mean y position of the bacterial trajectories. Errors denote SEM. Red and purple shaded area represent the region 3 μm from the LSW and RSW, respectively. Green shaded area represents the MA region. **E&F.** Normalized distribution of tumble angle for tracks along the sidewalls (**E**) and in the MA region (**F**). Red solid lines are fitting results with an exponential function: $y = a * \exp(x/b)$. **G.** Distribution of bacteria along the y-axis in the lanes with a width of 44 μm. The shades of different colors denote the same meaning as in Fig. 2D. **H.** Drift velocity of bacterial cells in the three regions. **I.** Proportions of bacterial trajectories in the three regions. Errors are standard deviations (SD).

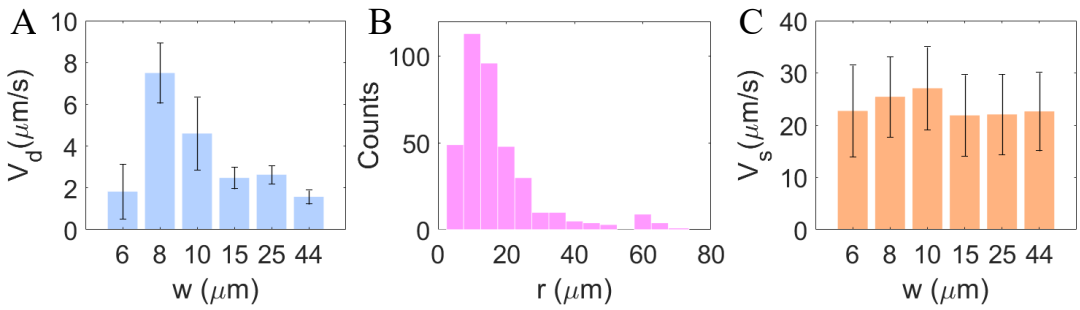

Fig. 3. **A.** The drift velocity for the experiments in lanes of different widths. The error in drift velocity is the standard deviation. **B.** The distribution of the radius of circular swimming from 382 trajectories in the MA regions. The peak value of the radius is ~10 μm. **C.** The swimming speed of cells in lanes with different widths. The mean swimming speeds and standard deviations for lanes with widths of 6 μm, 8 μm, 10 μm, 15 μm, 25 μm, and 44 μm are 22.7 ± 8.7 μm/s, 25.4 ± 7.7 μm/s, 27.1 ± 7.9 μm/s, 21.9 ± 7.8 μm/s, 22.1 ± 7.7 μm/s, and 22.6 ± 7.5 μm/s, respectively.

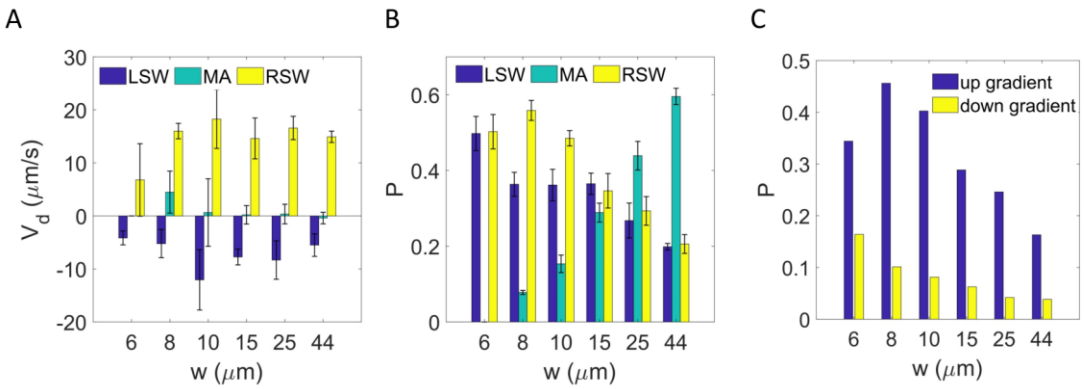

Fig. 4. **A.** Mean drift velocities in the LSW, MA, and RSW regions of lanes with different widths. The errors are SD. **B.** The proportion of bacterial cells in the LSW, MA, and RSW regions of lanes with different widths. Errors represent SD. **C.** The proportion of RSW-UG (cells swimming up-gradient in the RSW) and RSW-DG (cells swimming down-gradient in the RSW) for lanes with different widths.

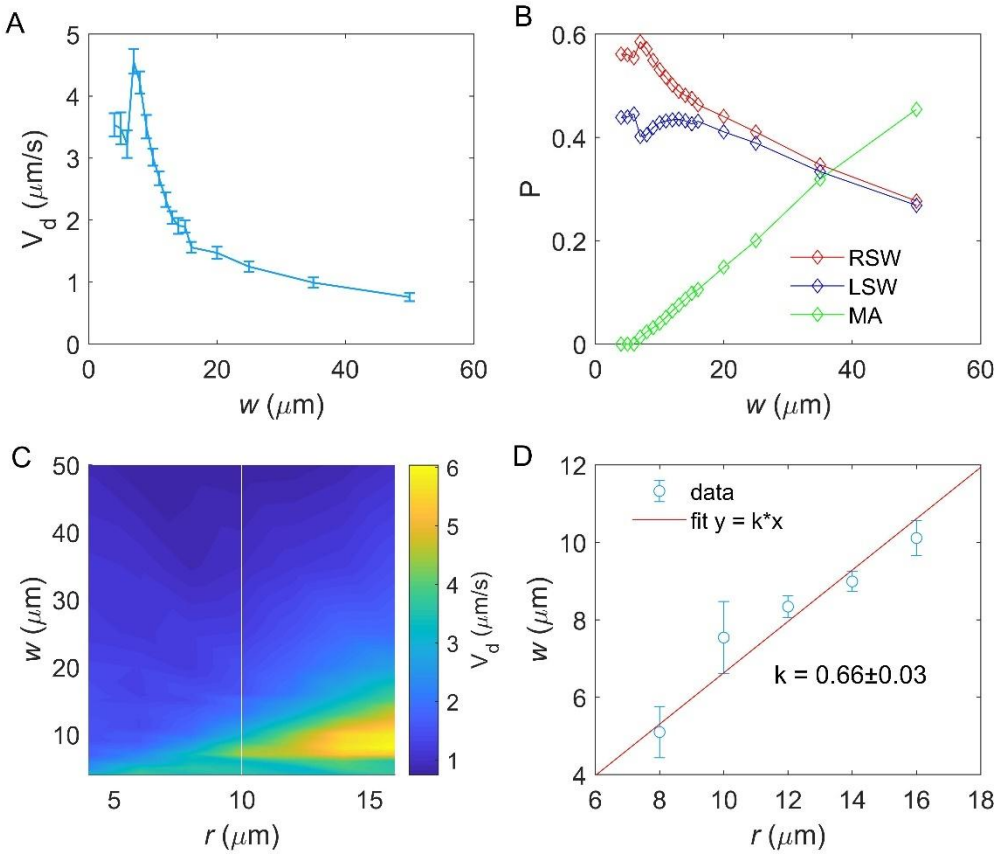

Fig. 5. Simulation of bacterial chemotaxis on the surface of lanes. **A.** The relationship between drift velocity V_d of cells with 10 μm-radius circular swim and the lane width w. Errors denote SEM. **B.** The proportion of bacterial trajectories in the LSW, MA, and RSW regions of lanes with different widths, for cells with 10 μm-radius circular swim. **C.** The drift velocity V_d of cells with different radii of circular swim in lanes of different widths. **D.** The relationship between circular swim radius and lane width for optimal chemotaxis (maximal drift velocity) in Fig. 5C. The widths were extracted by fitting the peak value of w in Fig. 5A with a gaussian function. The red solid line represents a linear fit. The slope is 0.66 ± 0.03. Errors denote SD.

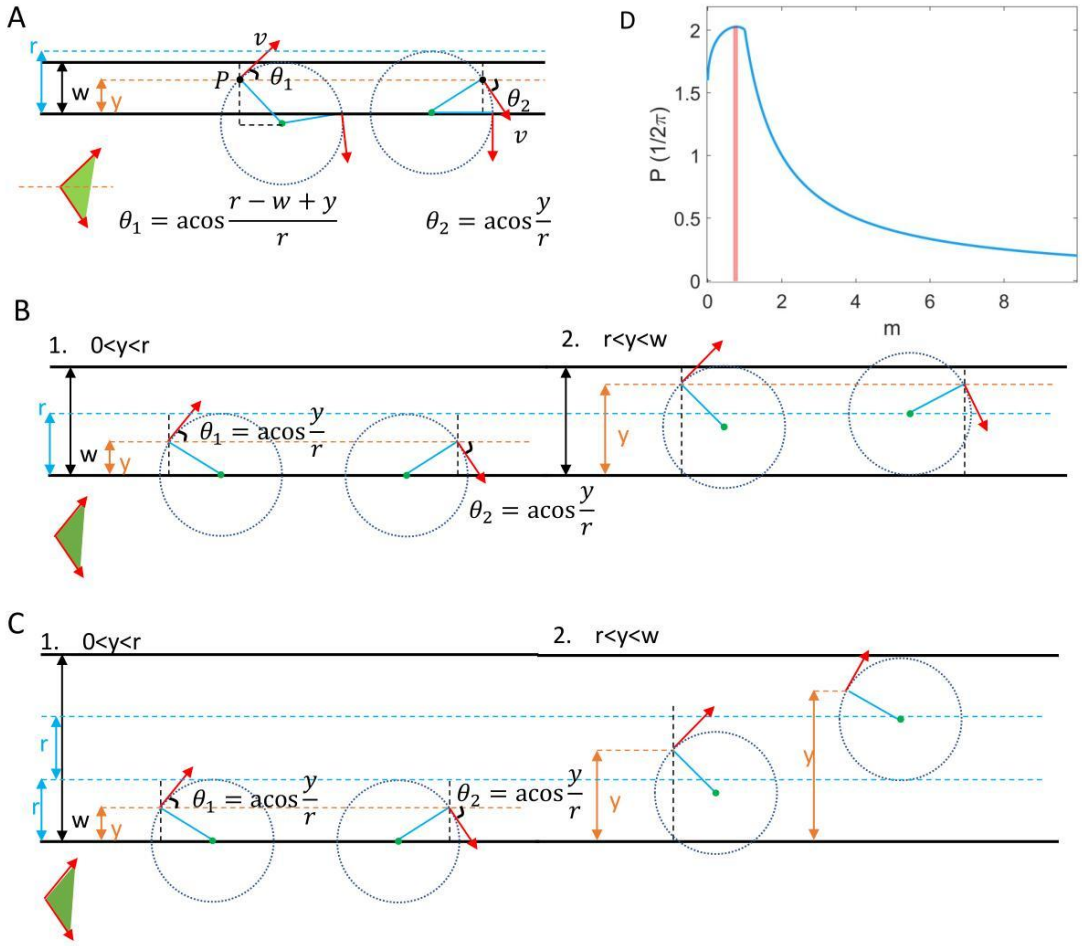

Fig. 6. Geometrical analysis of optimal lane width for chemotaxis. **A.** Case 1: $0 < w \leq r$. **B.** Case 2: $r < w \leq 2r$. **C.** Case 3: $w > 2r$. The red arrows denote the velocity direction. The black solid lines represent the sidewalls. Dashed circles are trajectories. The up-gradient direction is along the positive *x*-axis. The green shade areas label the swim direction of cells that can swim up-gradient in the RSW. **D.** Relationship between probability (*P*) of cells swimming up-gradient in the RSW and *m*, where *m* = *w*/*r*. Red shaded area denotes *m* for maximal *P*, $m \in (0.7, 0.8)$.

Supplemental materials

Explanation of difference in drift velocity between LSW and RSW cells.

We observed obvious chemotaxis of *E. coli* on the surface of lanes, closely related to cells swimming along sidewalls. As shown in Fig. S6A, cells swimming along sidewalls in an attractant gradient can be divided into four states: Cells on the right sidewall swimming up-gradient (RSW-UG), cells on the right sidewall swimming down-gradient (RSW-DG), cells on the left sidewall swimming up-gradient (LSW-UG), and cells on the left sidewall swimming down-gradient (LSW-DG). These cells can escape from sidewalls with rates:

$$k_{RSW-UG} = B^{+}k_{T}$$
$$k_{RSW-DG} = B^{-}k_{T} + (1 - B^{-})k_{R}$$
$$k_{LSW-UG} = B^{+}k_{T} + (1 - B^{+})k_{R}$$
$$k_{LSW-DG} = B^{-}k_{T}$$

where B^{+} and B^{-} represent the probability of tumble when cells swim up-gradient and down-gradient, respectively, and k_T and k_R denote the escape rates during tumble and run, respectively. Cells swimming on the sidewalls experience a force f_s from the bottom surface, causing them to swim to the right. RSW-UG and LSW-DG cells can swim away from the sidewalls via tumble, while RSW-DG and LSW-UG cells can escape via tumble or run. The gradient field direction ensures that $0 \leq B^{+} < B^{-} \leq 1$.

Dwell times for the four states are plotted in Fig. S6B, suggesting that $\tau_{RSW-UG} > \tau_{LSW-DG} > \tau_{RSW-DG} > \tau_{LSW-UG}$. Thus, $k_R > k_T > 0$. This is physically consistent: along sidewalls, running cells escape more easily via circular swimming, whereas tumbling cells are hindered by surface-suppressed reorientation and the high probability of tumbling back toward the sidewalls.

The drift velocity for cells on right and left sidewall can be calculated as:

$$v_d^{RSW} = v_0\left(\frac{1}{k_{RSW-RS}} - \frac{1}{k_{RSW-LS}}\right) = v_0\frac{(B^- - B^+)k_T + (1 - B^-)k_R}{B^+B^-k_T^2 + (1 - B^-)B^+k_Tk_R}$$

$$v_d^{LSW} = v_0\left(\frac{1}{k_{LSW-RS}} - \frac{1}{k_{LSW-LS}}\right) = v_0\frac{(B^- - B^+)k_T - (1 - B^+)k_R}{B^+B^-k_T^2 + (1 - B^+)B^-k_Tk_R}$$

where v_0 represents the swimming speed. Given that $0 \leq B^+ < B^- \leq 1$ and $k_R > k_T > 0$, we can conclude that:

$$v_d^{RSW} > 0$$
$$v_d^{LSW} < 0.$$

Supplemental movies

Movie S1. An example video of HCB1-pTrc99a-mCherry cells chemotaxis in a 44-μm-wide lane under a linear gradient of L-aspartate. The source channel is on the right side.

Movie S2. An example of a large reorientation angle during tumbling in the LSW of a 44-μm-wide lane under a linear gradient of L-aspartate. The source channel is on the right side. The cell of interest is marked with a blue circle.

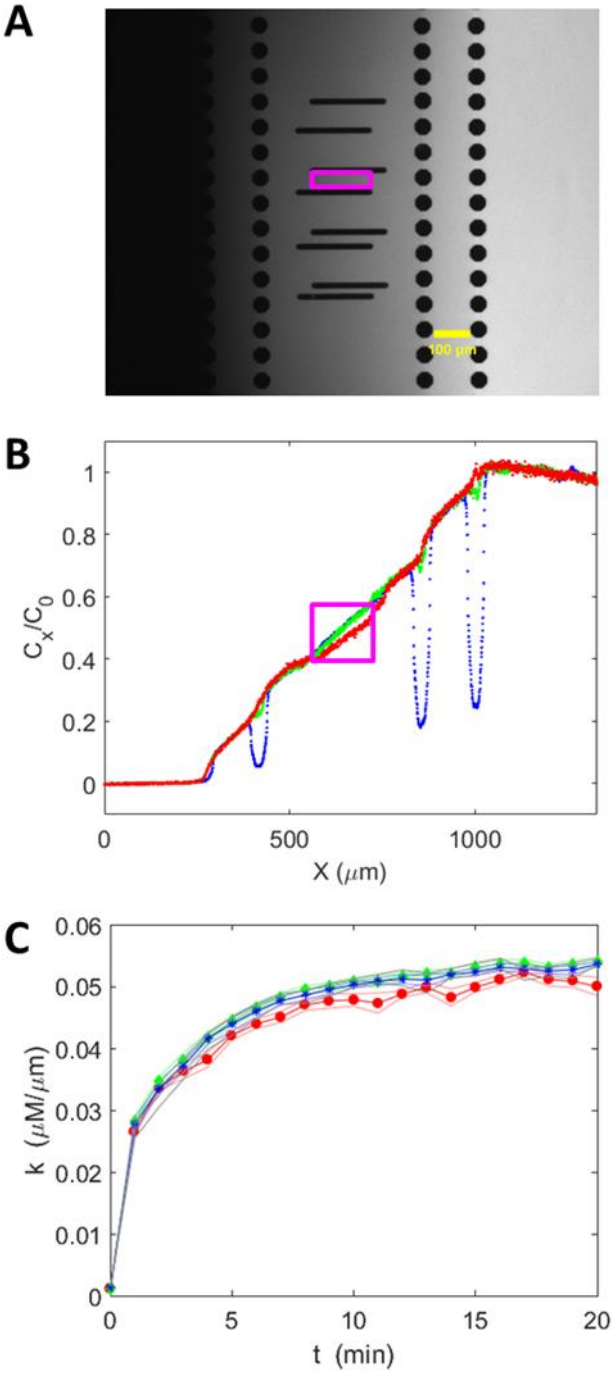

Fig.S1. Gradient calibration of microfluidics with fluorescein **A.** Fluorescence image of the stable gradient field. **B.** Normalized gradient in lanes of different widths. Red, green, and blue lines represent relative concentration values of the substance at different *x* positions for lanes with widths of 15 μm, 25 μm, and 44 μm, respectively. The red rectangle represents the ROI in Fig. S1A. **C.** Change in concentration gradient perceived by bacteria over time in lanes of different widths. Red circles (15 μm), green

diamonds (25 μm), and blue asterisks (44 μm) show 11 calibration measurements. Shaded areas represent SEM.

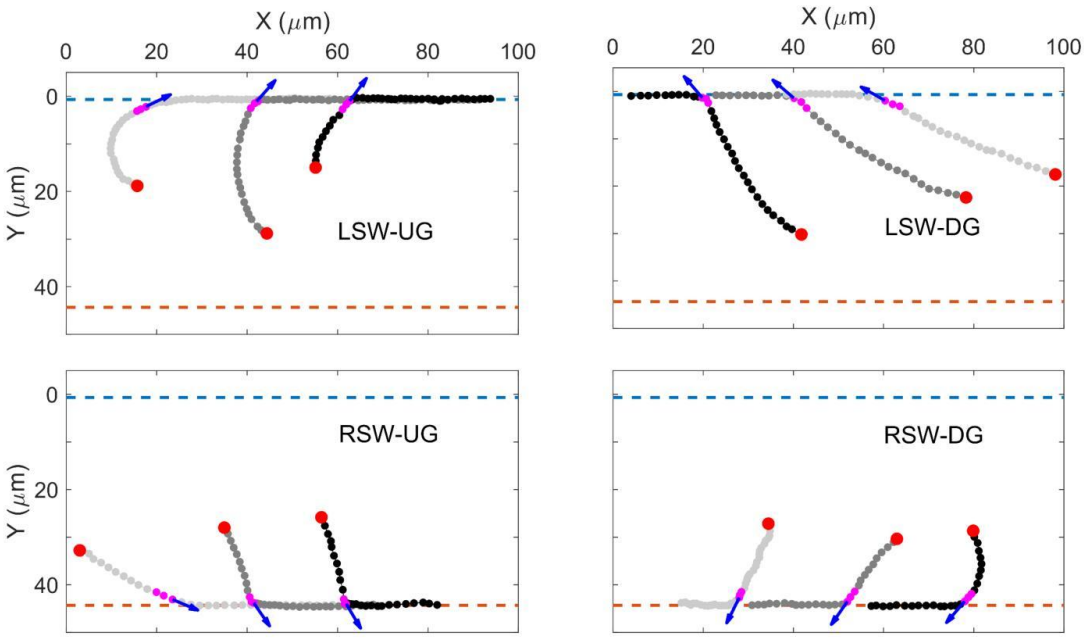

Fig. S2. Typical examples of collision trajectories between bacteria and sidewalls. Data are derived from the 44-μm-wide lane in gradient assays. Typical trajectories (gray dotted lines) illustrate cells colliding with the sidewalls, where different shades of gray represent distinct cells. The left and right sidewalls are indicated by blue and red dashed lines, respectively. Red points denote the starting positions of the trajectories, and blue arrows indicate the direction of the collision.

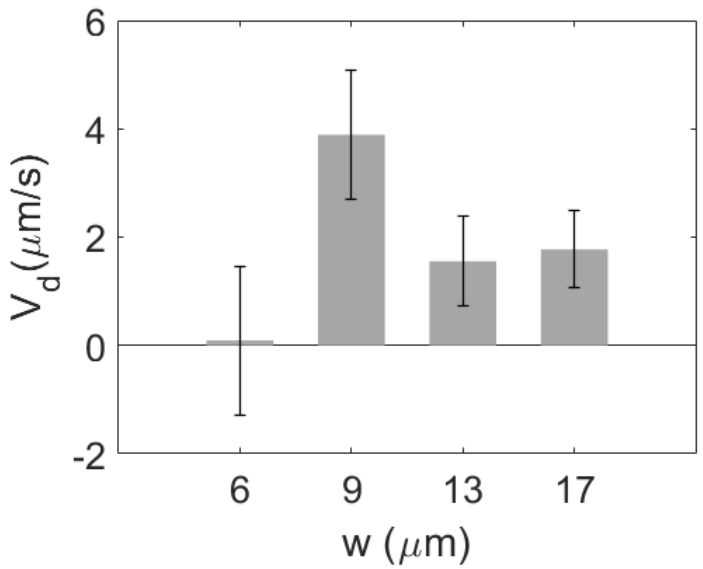

Fig. S3. The relationship between chemotactic drift velocity and channel width measured using a control setup with straight entrances. Channels with widths of 6, 9, 13, and 17 μm contain 217, 238, 434, and 538 trajectories, respectively. Error bars represent the standard deviation of the drift velocity.

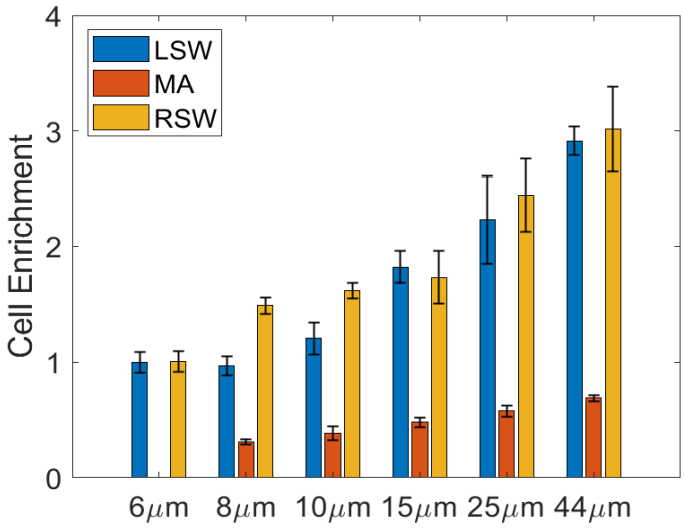

Fig. S4. The relationship between cell enrichment and lane width (w). Enrichment values are calculated by as $P \times w/3$ for LSW and RSW, and $P \times w/(w\text{-}6)$ for MA, where P represents the observed cell proportion from Fig. 4B.

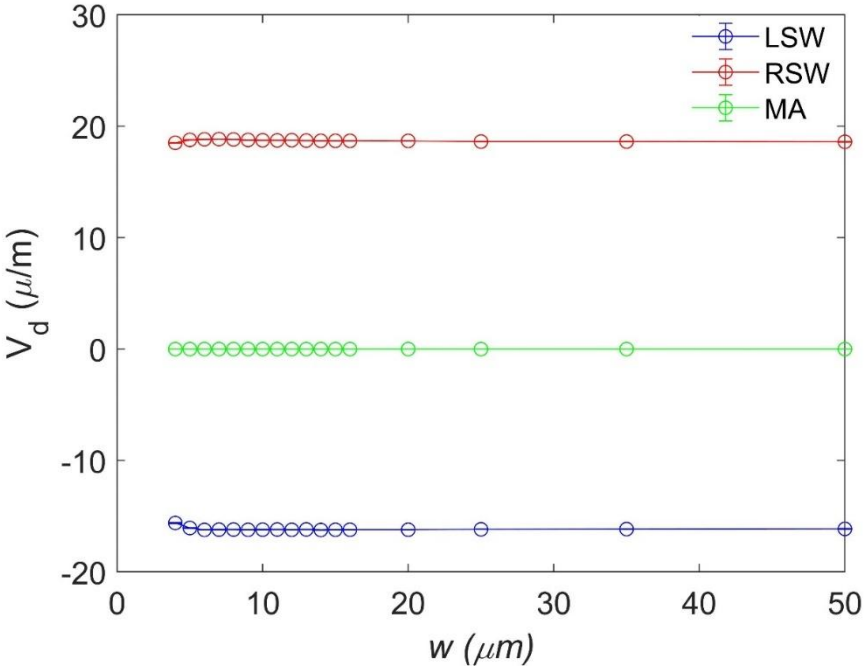

Fig. S5. Mean drift velocities in the LSW, MA, and RSW regions of lanes with different widths from simulations. The simulations assume cells perform a circular swim with a 10 μm radius.

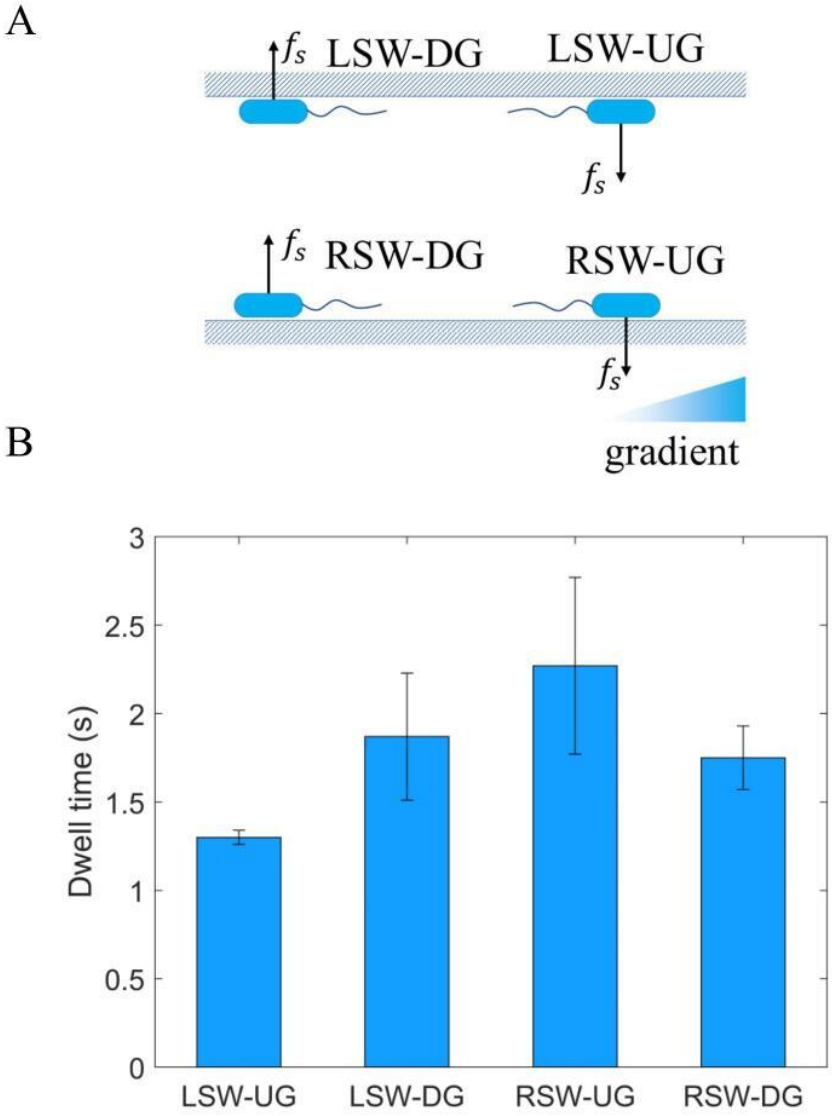

Fig.S6. **A.** Four motion states of cells swimming along sidewalls. Black arrows denote the direction of force f_s generated by the bottom surface on the cell body. **B.** Dwell times of the four motion states from experiments in 44 μm-wide lanes. The values are 1.3±0.04 s, 1.87±0.36 s, 2.27±0.5 s, and 1.75±0.18 s for LSW-UG, LSW-DG, RSW-UG, and RSW-DG respectively. Errors represent SDs.